OPEN ACCESS
IOP Publishing
Measurement Science and Technology
Meas. Sci. Technol. **30** (2019) 054003 (11pp)
https://doi.org/10.1088/1361-6501/ab0abc

Multiple scattering reduction in instantaneous gas phase phosphor thermometry: applications with dispersed seeding

Michael Stephan[1], Florian Zentgraf[1], Edouard Berrocal[2], Barbara Albert[3], Benjamin Böhm[1] and Andreas Dreizler[1]

[1] Institute for Reactive Flows and Diagnostics, Technische Universität Darmstadt, 64287 Darmstadt, Germany
[2] Division of Combustion Physics, Department of Physics, Lund University, SE-221 00 Lund, Sweden
[3] Eduard-Zintl-Institute of Inorganic and Physical Chemistry, Technische Universität Darmstadt, 64287 Darmstadt, Germany

E-mail: zentgraf@rsm.tu-darmstadt.de

Received 28 November 2018, revised 10 February 2019
Accepted for publication 26 February 2019
Published 10 April 2019

Abstract

In this study the structured laser illumination planar imaging (SLIPI) technique is combined with gas phase phosphor thermometry to measure quasi-instantaneously two-dimensional temperature fields with reduced bias from multiple scattering. Different reconstruction strategies are implemented, evaluated and compared, including a two-pulse and one-pulse SLIPI approach. A gradient-based threshold algorithm for particle detection is applied to conventional planar light sheet imaging as an alternative to reduce the bias caused by multiple scattering in seeding-free regions. As a demonstration, measurements are performed in a canonical flow configuration, consisting of a heated, turbulent, air jet surrounded by an ambient co-flow. Both air flows are seeded with the thermographic phosphor $BaMgAl_{10}O_{17}:Eu^{2+}$.

Conventional light sheet imaging in the context of gas phase phosphor thermometry suffers from multiple scattering causing a significant temperature bias and low temperature sensitivity. Applying the gradient threshold algorithm removes areas without any seeding particles which improves accuracy, precision and temperature sensitivity. However, multiple scattering influences are still present and may cause an increasing bias particularly for higher seeding density. One pulse (1p) SLIPI exhibits high accuracy at intermediate precision. Multiply scattered luminescence is not fully removed and spatial resolution is lowered. Two pulse (2p) SLIPI is recommended for high temperature sensitivity and accuracy, removing impact of multiple scattering furthermost. However, 2p-SLIPI exhibits reduced temperature precision.

Keywords: fluid thermometry, laser-induced phosphorescence, thermographic phosphor particles, multiple scattering, structured illumination

(Some figures may appear in colour only in the online journal)

1. Motivation and introduction

In mechanical, chemical and process engineering, fluid flow temperature is a vital parameter. Obtaining accurate temperature information is crucial for understanding the governing physical, chemical or even biological processes, for developing novel applications and for monitoring system operations. Examples span from combustion technologies to life science where temperature sensing is of crucial importance, as in living cells [1, 2] or *in vivo* thermometry [3] explored for disease detection in biomedical hosts.

Optical laser diagnostics provide the capabilities for minimal invasive, simultaneous multi-parameter measurements at high spatial and temporal resolution. In the past decades, numerous laser diagnostics for fluid thermometry have been proposed, e.g. coherent anti-Stokes Raman spectroscopy (CARS) [4], Rayleigh thermometry [5], tunable diode laser absorption spectroscopy (TDLAS) [6], laser-induced fluorescence (LIF) [7] or laser-induced luminescence (LIL) applied to thermographic phosphors [8–10]. Each technique has its specific advantages and disadvantages. Especially the LIL-approach is very promising by its combination with particle image velocimetry (PIV). In this concept, the dispersed thermographic phosphor (TGP) particles serve as tracers for both velocimetry and thermometry [11–14].

TGPs consist of ceramic host materials doped with luminescence active rare-earth or transition metal ions [9, 11]. Laser-induced excitation is in the ultraviolet, while the temperature-sensitive emission is typically in the visible spectral range [11]. Depending on temperature, intensity and spectral distribution of the luminescence emission as well as the temporal decay time vary. These properties are utilized for temperature sensing. Wall thermometry using TGPs was reviewed by Aldén *et al* [8] and Brübach *et al* [9] and fluid thermometry by Abram *et al* [10]. For fluid phase thermometry applications, the TGP tracer is dispersed as seeding powder into the flow (individual particle size several µm). In the study presented here, the phosphor $BaMgAl_{10}O_{17}:Eu^{2+}$ (BAM) is used [15, 16], common in gas phase phosphor thermometry [11, 12, 14, 17].

Previous investigations indicated that multiply scattered luminescence emission originating from seeding particles can strongly bias temperature measurements [12, 13, 17, 18]. Three primary mechanisms of multiple scattering were identified:

(i) Luminescence emission originating from the illuminated plane is multiply scattered and emits to the camera from off-plane locations.
(ii) Incident laser light is multiply scattered to off-plane locations and excites luminescence, emitting to the camera.
(iii) Incident laser light is multiply scattered to off-plane locations and excites luminescence that is subsequently multiply scattered prior to detection.

Two major effects on phosphor thermometry need to be considered. First, blurred signals originating from multiple scattering are observed within the entire image, also in seeding-free areas. Second, local temperature information is mixed.

Multiply scattered light and the resulting effects can be suppressed applying a structured illumination approach designed for macroscopic flow systems called structured laser illumination planar imaging (SLIPI), introduced to fluid mechanics by Berrocal *et al* [19] and Kristensson *et al* [20]. SLIPI is based on recording multiple sub-images resulting from spatially intensity modulated light sheets at different spatial phase shifts. The modulation pattern is retained by signal photons that are not multiply scattered ('un-scattered'), while multiply scattered light is loosing this structure, appearing as blurred offset. By SLIPI post-processing, multiple scattering contributions can be mitigated. This technique has demonstrated its capabilities in numerous applications in the past and has advanced over the years. Related to the number of sub-images recorded by p pulses, three different approaches are distinguished:

(i) 1p-SLIPI, based on one spatially modulated image;
(ii) 2p-SLIPI, using two spatially modulated sub-images, phase-shifted to each other by 180°;
(iii) 3p-SLIPI, based on three spatially modulated sub-images, with phases of 0°, 120° and 240°, respectively.

The original three pulse (3p) approach was developed for time-averaged measurements in dense sprays [19] and further advanced in [21] for freezing rapid flow motion. Two-pulse [22–24] as well as one-pulse SLIPI [24, 25] applications were demonstrated, simplifying the experimental complexity and cost. SLIPI was combined with various laser optical diagnostics like LIF/Mie droplet sizing [23, 26], LIF thermometry [27], Rayleigh thermometry [28, 29] and PIV [30]. A first combination of SLIPI with gas phase phosphor thermometry (SLIPI-LIL) was presented in [18] for time-averaged temperature field measurements.

This study extends the previous SLIPI-LIL approach to quasi-instantaneous temperature field measurements in gaseous flows. A novel particle identification algorithm is introduced to distinguish signal contribution originating from multiple scattering in seeding-free regions. However, multiple scattering superimposed to particles is not suppressed by this algorithm, but only in non-seeded areas. For purpose of demonstration, investigations are performed in a canonical jet and co-flow configuration using the common phosphor $BaMgAl_{10}O_{17}:Eu^{2+}$ (BAM) as tracer [11, 12, 14–17]. The capability of 1p- and 2p-SLIPI-LIL gas phase thermometry is benchmarked against the conventional approach, considering temperature sensitivity, accuracy and precision of each reconstruction technique.

2. Description of the optical techniques

To assess the influence of multiple light scattering on quasi-instantaneous gas phase thermometry, laser-induced luminescence (LIL) thermometry and structured laser illumination

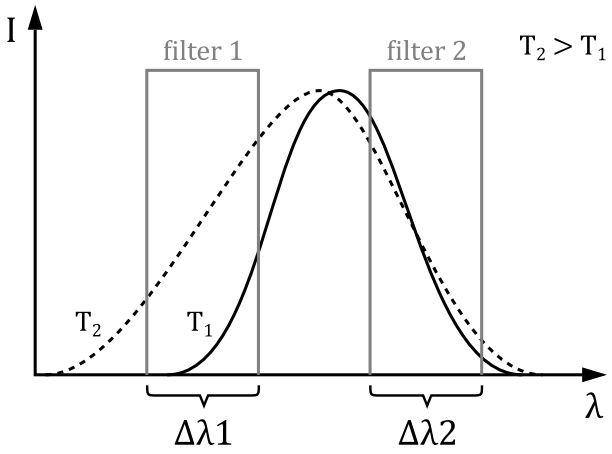

Figure 1. Thermometry using two-color ratio laser-induced luminescence (LIL). Normalized luminescence emission spectra shown.

planar imaging (SLIPI) are combined. This section summarizes the fundamentals of these techniques.

2.1. Laser-induced luminescence thermometry

For two-dimensional gas phase thermometry based on laser-induced luminescence, a two-color ratio technique is employed. This approach derives a temperature dependent ratio

$$R(T) = \frac{I_{\Delta\lambda1}(x,y)}{I_{\Delta\lambda2}(x,y)} = C \cdot \frac{\Phi_{\Delta\lambda1}}{\Phi_{\Delta\lambda2}} \tag{1}$$

by dividing the two-dimensional images $I(x,y)$ simultaneously recorded at two different spectral ranges $\Delta\lambda1$ and $\Delta\lambda2$ of the luminescence emission spectrum [9, 12]. The concept is outlined in figure 1. Ideally, one spectral range $\Delta\lambda$ is not influenced by temperature variations while the other range features a pronounced temperature dependency. The intensities I are spectrally integrated within their respective spectral ranges and temporally integrated across their temporal luminescence decay. In equation (1) influences like laser fluence, number of particles in the probe volumes or absorption cross section cancel each other. According to Lee *et al* [12] the ratio reduces to the respective quantum yields Φ of the luminescence process, specifying the number of luminescence photons emitted in $\Delta\lambda1$ and $\Delta\lambda2$, and a calibration constant C. Thus, for conversion of the two-color ratios R to temperatures T, an *in situ* calibration is required. Additionally, background radiation and vignetting must be corrected for [8, 10].

2.2. Structured laser illumination planar imaging for multiple scattering reduction

Structured laser illumination planar imaging (SLIPI) has been established as a suitable concept for reducing multiple light scattering in flow diagnostics. SLIPI is based on recording of multiple sub-images I_n resulting from n spatially intensity modulated laser light sheets at different spatial phase

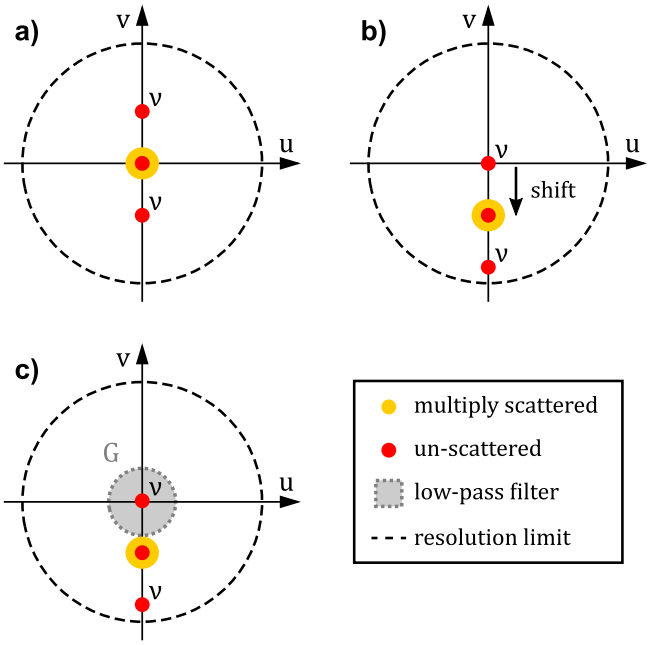

Figure 2. Fourier transformation of (a) sub-image I_0, initial state for 1p-SLIPI; (b) shift of Fourier spectrum; (c) application of low-pass filter; *G*: low-pass filter.

shifts ($\Delta\varphi = 2\pi/n$) [19]. Multiply scattered photons do not retain the modulation of the incident laser light sheets in the recorded sub-images, while undisturbed photons do [19]. This allows to distinguish between multiple and un-scattered photons via image post-processing such that the desired in-plane signal, i.e. SLIPI image I_{SLIPI}, can be extracted. In order to preserve spatial resolution, the original SLIPI approach was based on $n = 3$ sub-images for image reconstruction [19]. This approach is well-suited for averaged imaging. For instantaneous imaging [21], 3p-SLIPI requires costly equipment and careful optical alignment. As this study aims at providing instantaneous images with more affordable equipment, the one pulse (1p) and two pulse (2p) SLIPI approaches have been chosen. Both approaches are briefly outlined in the following. 2p-SLIPI requires two modulated laser light sheets with half a modulation period spatial phase shift ($\Delta\varphi = \pi$), resulting in the sub-images I_0 and I_π [22]. For the 2p-SLIPI reconstruction, sub-images are subtracted from each other ($I_{\mathrm{2p-SLIPI}} \propto I_0 - I_\pi$), thereby removing the multiply scattered intensity I_{MS} [22]. The 2p-SLIPI approach contains residual line structures in the resulting $I_{\mathrm{2p-SLIPI}}$ [22], decreasing its spatial resolution. By summation of both images a so-called conventional image results ($I_{\mathrm{conv}} \propto I_0 + I_\pi$), equal to an image originating from classical planar laser imaging without spatial modulation and resolution losses but biased by multiple scattering. In the following, I_{conv} is used as a benchmark to evaluate the results from SLIPI reconstructions.

The 1p-SLIPI approach by Mishra *et al* [24] aims for even further reducing experimental and post-processing efforts. Multiple scattering is suppressed using only one sub-image (either I_0 or I_π, here: I_0). The main idea of 1p-SLIPI is that multiple scattering blurs the images such that its influence is characterized by low spatial frequencies. Transforming an

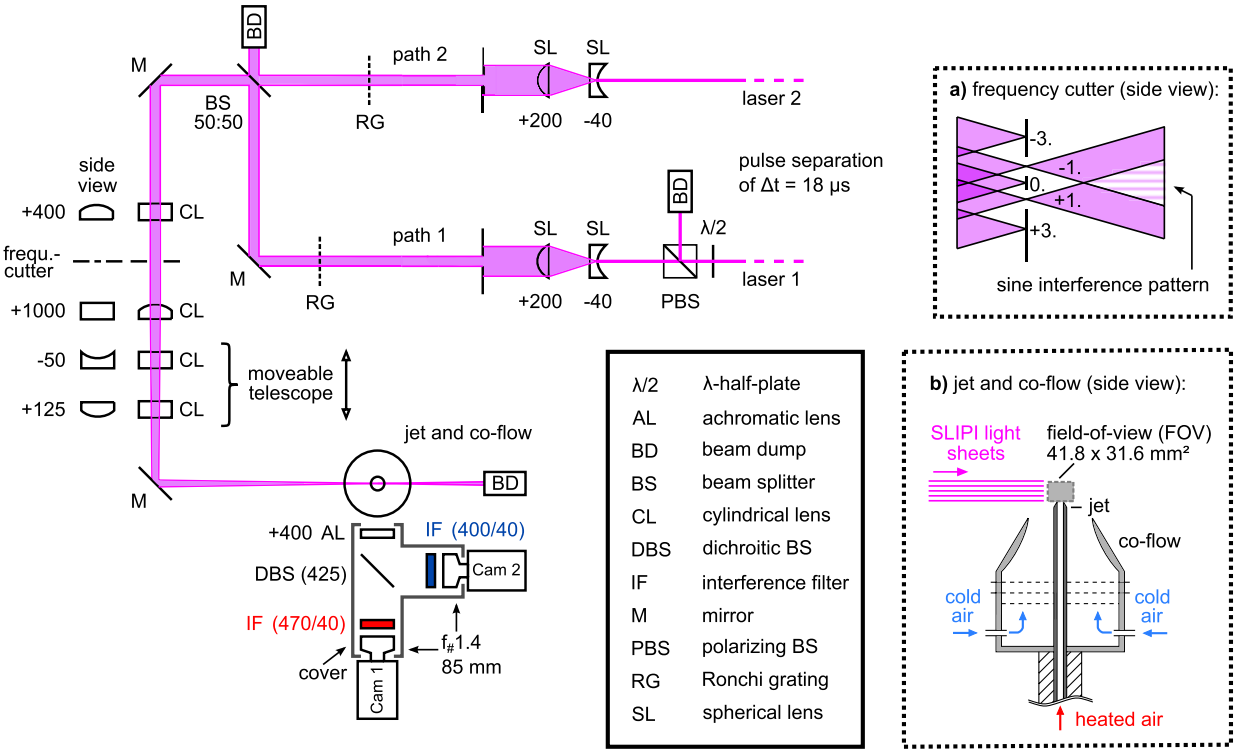

Figure 3. Experimental setup for quasi-instantaneous SLIPI-LIL gas phase thermometry.

intensity modulated sub-image I_0 to its Fourier space ($\mathcal{F}$), two prominent features are observed, as shown in figure 2(a): (1) a component centered at the origin of the Fourier space representing the averaged image intensity [31]; (2) a component at frequency ν corresponding to the modulation frequency of the SLIPI light sheet. The majority of multiply scattered light is located in the central part of the Fourier spectrum at low frequencies. By applying a modulation, the un-scattered information is duplicated around this frequency (ν, see figure 2). Thus, by using a sufficiently high frequency ν, the desired un-scattered information can be isolated from most of the multiple light scattering component. Photons that are not multiply scattered preserve the intensity modulation of the light sheet, thus, signal contained in the frequency component ν corresponds to signals unbiased by multiple scattering. For reconstruction, two different approaches are common [24]: the *lock-in detection* and the *detection of the first-order peak*. Here the latter approach is followed as outlined in figure 2(b). The entire Fourier spectrum is shifted in the v-direction to offset one ν component to the center [24]. A low-pass filter G is applied removing the averaged intensity contribution which contains multiply scattered light (see figure 2(c)). By back-transformation to physical space, the filtered image $I_{1p-SLIPI}$ is significantly less influenced by multiple scattering. The inverse Fourier-transformation ($\mathcal{F}^{-1}$) is mathematically expressed by

$$I_{1p-SLIPI} \propto \mathcal{F}^{-1}\left\{\mathcal{F}\left\{I_0(x,y)\right\}(u,v-\Delta v)\cdot G\right\}, \quad (2)$$

where u and v are spatial frequencies and G is the low-pass filter in the frequency domain.

Note, that $I_{2p-SLIPI}$, $I_{1p-SLIPI}$ and I_{conv} all can be calculated from the *identical* pair of quasi-simultaneous raw sub-images I_0 and I_π. This allows for a direct comparison and evaluation of these approaches.

3. Experimental methodology

The combination of quasi-instantaneous two-color ratio LIL thermometry and SLIPI is applied to a canonical jet in co-flow configuration. The experimental setup of this study is shown in figure 3.

3.1. Flow configuration

The canonical flow configuration introduced in [12] and [18] consists of a circular jet (16 mm diameter), surrounded by a co-flow of 140 mm in diameter (side view in figure 3(b)). Jet and co-flow are operated with air seeded with TGP particles of $BaMgAl_{10}O_{17}:Eu^{2+}$ (BAM, Phosphor Technology Ltd., KEMK63/UFP2). The jet is heated and operated in the turbulent regime (Re = 6400), while the co-flow is at ambient temperature and laminar conditions (bulk velocity $\approx$0.2 m s^{-1}). The flow configuration is operated in steady-state and controlled by commercial mass flow controllers (Bronkhorst High-Tech). Flow temperatures are continuously monitored using type K thermocouples.

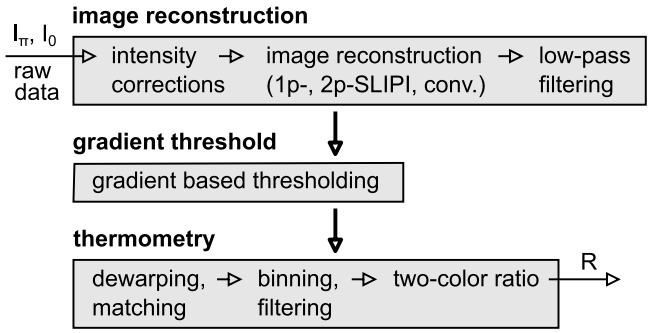

Figure 4. Workflow of data post-processing.

3.2. Laser optical setup

The laser optical setup shown in figure 3 is designed to perform quasi-instantaneous two-dimensional 2p-SLIPI-LIL gas phase thermometry measurements.

Two independent laser pulses are provided by two Q-switched Nd:YAG lasers (third harmonic at 355 nm, 5 Hz repetition rate). The time separation between both laser pulses is 18 µs, resulting in quasi-instantaneous temperature field measurements. This value is chosen exceeding the ≈2 µs lifetime of BAM at ambient conditions [16] to avoid any bias from sequential excitation of the TGP particles. The two laser pulses are passing individual Galilean telescopes and rectangular apertures to select beam regions with approximately homogeneous laser intensity. The Ronchi gratings (Edmund Optics, 5 line pairs/mm) create individual diffraction patterns for each beam path. The spatial phase shift between both modulated SLIPI light sheets is aligned by vertically shifting one of the Ronchi gratings [18]. Both pulses are overlapped and focused on a so-called frequency cutter device (side view in figure 3(a)), which selects both ±1st diffraction orders while blocking all remaining orders. By overlapping these two resulting coherent beams after the frequency cutter, a sinusoidal beam profile is generated by interference, finally resulting in a SLIPI laser light sheet. This method to generate the sinusoidal modulated light sheet pattern is called fringe projection [32]. Light sheets are shaped regarding modulation period and thickness using cylindrical lenses prior to entering the field-of-view (FOV). Within the FOV, the SLIPI light sheets are 285 ± 45 µm thick and have a modulation period of 270–330 µm. Average laser pulse energies are 0.43–0.52 mJ with 15–22 µJ standard deviation (energy statistics based on 500 single laser pulses).

The resulting laser-induced luminescence is collected by an achromatic lens and spectrally separated by a dichroitic beam splitter (Chroma Technology Corp., T425LPXR) into a *blue* ($\lambda < 425$ nm, reflected) and *red* channel ($\lambda > 425$ nm, transmitted), corresponding to $\Delta\lambda 1$ and $\Delta\lambda 2$ in equation (1). To more accurately define the spectral ranges, additional bandpass interference filters (Chroma Technology Corp., compare figure 3 for center wavelength/full width half maximum) are placed in front of each objective lens (f-number $f_\#$ 1.4, focal length 85 mm). Each channel is recorded by an individual interline-transfer CCD camera (PCO AG, sensicam qe double shutter). Both cameras were operated in a double shutter mode. The first frame (5 µs exposure time) records sub-image I_0, the second subsequent frame (nearly 100 ms exposure time, limited by readout time of the first frame) captures I_π. To avoid any bias from ambient background in I_π, the camera system is shuttered by a box and the ambient light is switched off during recordings. Recordings are performed with 5 Hz repetition rate. The entire measurement system is synchronized using a digital delay pulse generator (Quantum Composers Inc.).

4. Data post-processing

Data post-processing for deriving quasi-instantaneous two-dimensional temperature fields consists of three steps. The workflow is outlined in figure 4. First, an image reconstruction post-processing is executed. Second, a gradient based threshold criterion is applied to the reconstructed images to exclude any bias from seeding-free regions. Finally, a thermometry routine converts intensity information into temperature information. All procedures are implemented in MATLAB R2016a (The MathWorks, Inc.).

4.1. Image reconstruction

The image reconstruction algorithm provides three alternative ways to process the raw sub-images I_0 and I_π according to the outlines in section 2.2: (1) the conventional I_{conv}, (2) the 2p-SLIPI $I_{\mathrm{2p-SLIPI}}$ and (3) the 1p-SLIPI reconstruction $I_{\mathrm{1p-SLIPI}}$. All image reconstructions are based on an *identical* pair of quasi-simultaneous raw sub-images I_0 and I_π and are done for the blue and red camera channel separately, using the identical algorithms.

The conventional and 2p-SLIPI reconstruction are using both sub-images I_0 and I_π. A more detailed description of the algorithmic implementations of these reconstructions is given in [18]. The procedure is briefly summarized in the following. Initially, intensity correction steps are performed, compensating for temporal and spatial intensity fluctuation between the sub-images, e.g. originating from the laser or fluctuating seeding densities. In a subsequent step, the two sub-images are reconstructed via addition to a conventional image I_{conv} or subtraction to a SLIPI image $I_{\mathrm{2p-SLIPI}}$ (section 2.2). Finally, low-pass filtering is applied to remove residual line structures inherently resulting in the 2p-SLIPI approach. For consistency, this is equally performed for I_{conv}.

1p-SLIPI is based on using only the sub-image I_0. Following the procedure outlined in section 2.2, the sub-image is transfered to the frequency domain using a fast Fourier transformation (FFT). The upper frequency component ν (figure 2) is shifted to the center of the Fourier domain (MATLAB function `circshift`). A second order Butterworth low-pass filter is applied to remove all frequency components except the centered ν-component, mainly containing light not biased by multiple scattering. After filtering, the image is finally transformed back to the physical space using an inverse FFT.

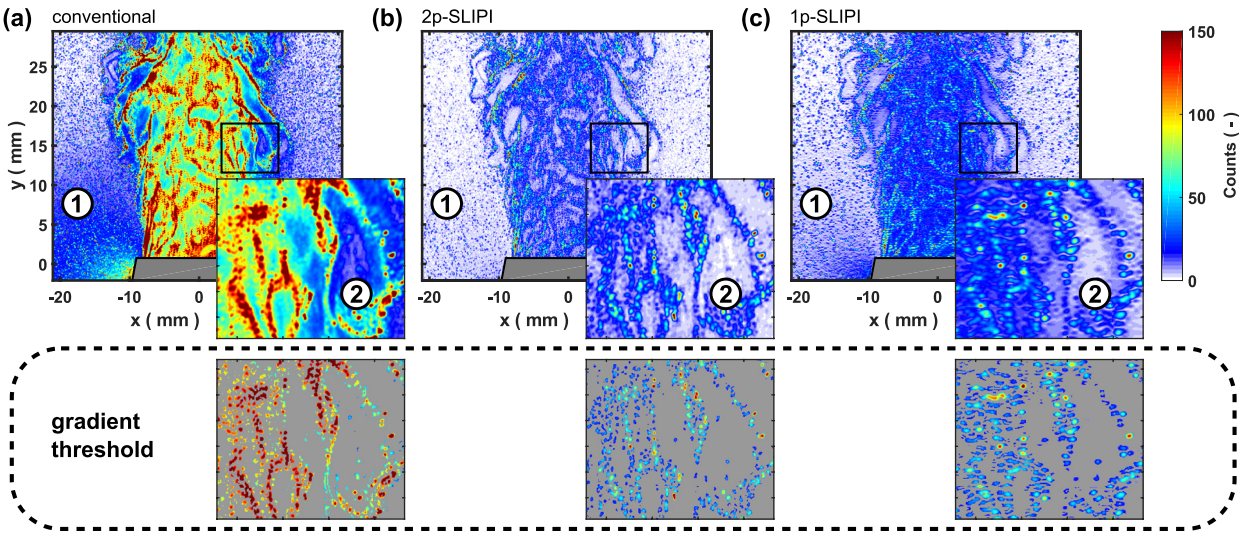

Figure 5. Two-dimensional count images of different reconstruction approaches: (a) conventional, (b) 2p-SLIPI, (c) 1p-SLIPI with zoomed views. Zoomed top row: no threshold applied, zoomed bottom row: gradient threshold applied (excluded background colored gray for better contrast). Instantaneous single-shot image shown for the red camera channel.

4.2. Gradient threshold

In gas phase TGP thermometry, the desired temperature information is emitted from individual seeding particles. Consequentially, seeding-free areas must be removed. Signal observed in those areas is attributed to multiple scattering or wall reflections. Zones with no seeding need to be excluded from further processing. For this purpose, a gradient based threshold algorithm is applied to the reconstructed images, distinguishing between seeded and non-seeded regions. The algorithm uses approximated first and second order derivatives to separate particles from their background [33]. More details are presented in the appendix. In the case of 2p-SLIPI, the gradient based threshold criterion is complemented by using a subsequent global thresholding. The global thresholding considers absolute count values ($I(x,y) > T_0$ with empirical T_0). This was required in the case of 2p-SLIPI to remove a remaining low-signal *corona* surrounding individual particles. Furthermore, this ensured sufficiently high signal levels for further processing.

4.3. Thermometry

In the last step temperature fields are derived from the reconstructed and thresholded images [18]. The reconstructed blue and red channel images are physically matched on a pixel-by-pixel base to ensure an accurate calculation of the two-color ratio. The matching is performed in two steps. First, the individual images are dewarped using correction polynomials calculated from calibration target recordings by DaVis (LaVision GmbH). Second, MATLAB algorithms for image warping are applied. Subsequently, a software-binning is performed to increase the signal-to-noise ratio (6×6 for conventional and 2p-SLIPI, 10×10 for 1p-SLIPI). This results in a final spatial resolution of 180 µm for the conventional and 2p-SLIPI approach and 320 µm for 1p-SLIPI. The spatial resolution of 1p-SLIPI is limited by the required low-pass filtering in the Fourier space that is inherently determined by the modulation frequency ν of the SLIPI light sheet (see figure 2). In this study, the experiment and thus the modulation frequency ν is designed for a 2p-SLIPI realization [22] such that 2ν is close to the resolution limit of the detection system. This limits the spatial resolution of 1p-SLIPI here. In general, a high spatial modulation frequency ν is essential for the spatial resolution in 1p-SLIPI [24]. The two-color ratio is calculated by dividing the blue and red channel images pixel-by-pixel. A flat-field correction is performed and finally a conversion to temperature fields is done by applying the calibration curves.

5. Results and discussion

Results of different quasi-instantaneous SLIPI-LIL thermometry approaches are presented and discussed in terms of reconstructed images, calibration curves, temperature fields, accuracy, precision and signal-to-noise ratio (SNR).

5.1. Image reconstruction

Results from different image reconstructions shown in figure 5 are evaluated regarding their apparent multiple scattering impact. For discussion, zoomed regions of the shear layer between jet and co-flow are considered using only the red camera channel. The blue channel features similar characteristics and is not shown here. The emphasis in this discussion is on the effect of the applied gradient threshold criterion (zoomed view in figure 5 top row: no threshold applied, bottom row: gradient threshold applied).

Without applying thresholding the conventional case (figure 5(a)) is strongly affected by multiple scattering as evident from rather high signal levels in areas where apparently no seeding particles are present. 2p-SLIPI (figure 5(b)) is capable to remove most of the multiple scattering evident from a high contrast observed between particles and background.

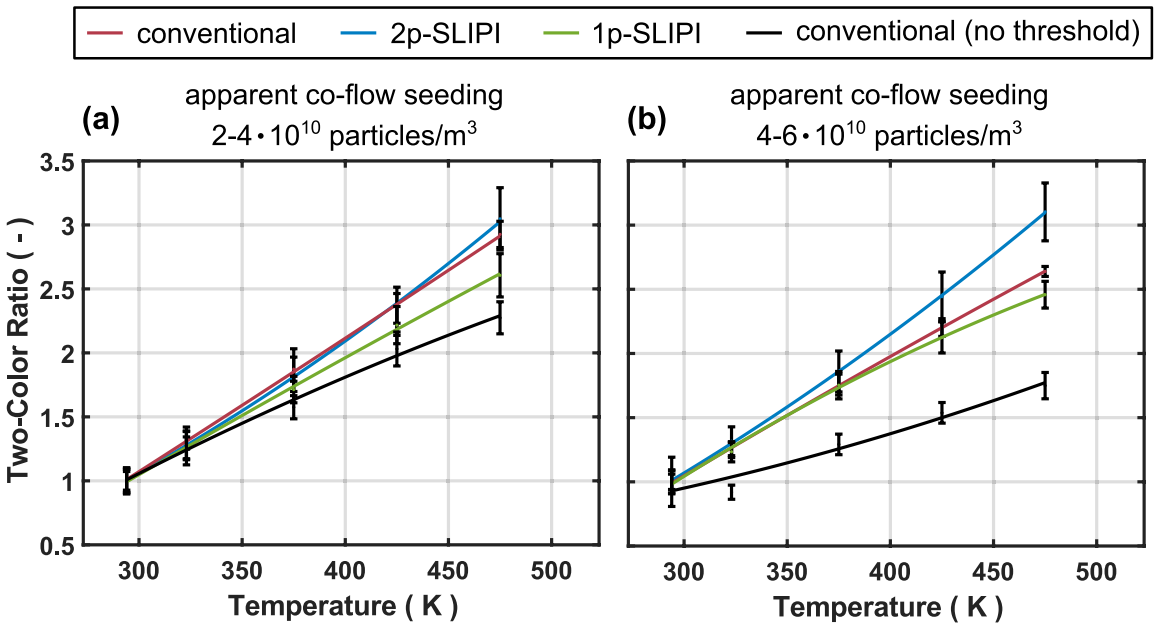

Figure 6. Calibration curves for quasi-instantaneous SLIPI-LIL thermometry at different apparent co-flow seeding densities 2–4 · 10^{10} particles m^{-3} (left), 4–6 · 10^{10} particles m^{-3} (right).

Compared to 2p-SLIPI the 1p-SLIPI (figure 5(c)) approach apparently features a less efficient suppression of multiple scattering. This is evident from inspecting zones where the laser sheets hit the jet nozzle, creating bias by wall-bounded luminescence (particles sticking at the wall) and backscattering into the co-flow (figure 5 ①) or from individual vortices that are free of any seeding (figure 5 ②).

Particularly, vortical structures containing areas without any seeding particles illustrate the need for particle identification, as feasible with the applied gradient threshold algorithm. Comparing images with and without thresholding for the conventional case (figure 5(a)) shows that areas not containing any seeding particles exhibit significant signal levels (5–40 counts in the shear layer, above 60 counts in the jet core) that furthermore possess strong local variations. These apparent signals are related to multiple scattering and cause a significant bias. Thus, seeding-free areas need to be excluded. In the 2p-SLIPI reconstruction, the seeding-free zones exhibit low signal up to five counts (shear layer as well as jet core) at very high spatial homogeneity. The 1p-SLIPI features 5–10 remaining counts in the seeding-free zones and up to 15 counts in the jet. Here, the local variations are more pronounced compared to the 2p approach.

Results presented in the following are further processed using the gradient-thresholded raw images. However, the non-thresholded conventional case is still used as a 'worst case benchmark'.

5.2. Temperature quantification of luminescence signal

To derive temperatures from the recorded luminescence signals using two-color ratios, an *in situ* calibration procedure is required. The calibration is linking the computed two-color ratios with temperatures measured here with a thermocouple (type K, 1.5 mm diameter). Calibration curves for quasi-instantaneous SLIPI-LIL thermometry are shown in figure 6 for the different image reconstruction procedures and varying apparent co-flow seeding densities. The 2p-SLIPI approach features highest temperature sensitivity, followed by the gradient-thresholded conventional, 1p-SLIPI and finally the non-thresholded conventional approach. The reduced sensitivity of 1p-SLIPI compared to the gradient-thresholded conventional originates from low-pass filtering in the Fourier space image processing. 1p-SLIPI derived from sub-images originally designed for 2p-SLIPI applications inherently requires strong filtering, thus smoothing more strongly particle signal intensities with surrounding background or multiply scattered signal. 2p-SLIPI appears to be very robust against varying seeding densities in the co-flow, i.e. an increased multiple scattering level (compare blue curves in figures 6(a) and (b)). This is in contrast to the other approaches. Particularly, the non-thresholded conventional approach is strongly dependent on the seeding density such that calibration and subsequent measurement of unknown temperature fields must be conducted for similar seeding densities. In practice, this is often difficult to achieve.

5.3. Temperature fields

Based on the identical raw data, figure 7 shows typical two-dimensional, quasi-instantaneous temperature fields using the different reconstruction approaches. For discussion, zoomed regions of the shear layer between jet and co-flow are considered. Temperature fields are calculated using the respective calibration curves shown in figure 6(a). For the operation conditions shown, the jet core temperature was set to 453 K. As worst case benchmark, the temperature field derived from a non-thresholded conventional reconstruction is shown in

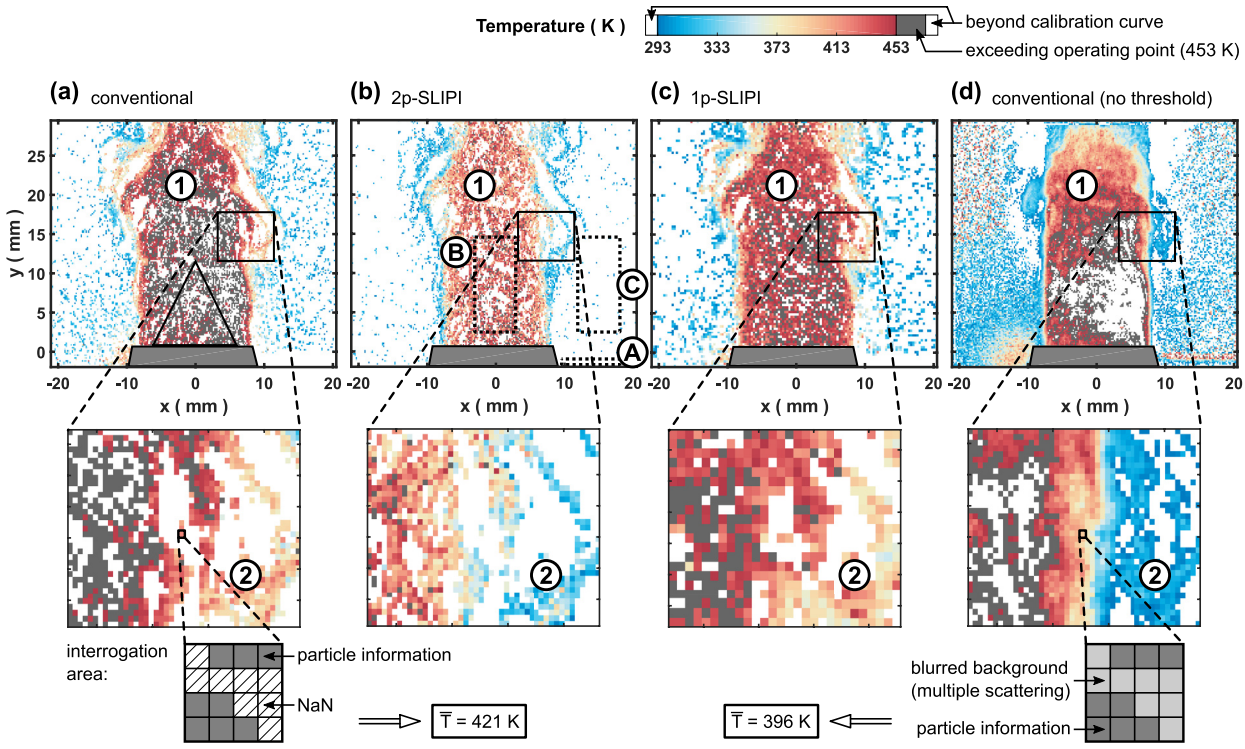

Figure 7. Two-dimensional, quasi-instantaneous temperature fields for different reconstruction approaches: (a) conventional, (b) 2p-SLIPI, (c) 1p-SLIPI, (d) non-thresholded conventional. Temperatures beyond calibration curve values ($T < 294$ K, $T > 475$ K) and areas without particles: white; temperatures exceeding the operating point 453 K but within the range of calibration curves: gray.

figure 7(d). Additionally, the bottom row of figure 7 includes schematics to describe the impact of the applied gradient thresholding. For thermometry, signals of individual pixels need to be binned to interrogation areas prior to two-color ratio calculation (section 4.3), resulting in locally averaged temperatures $\overline{T}$. In the thresholded cases (figures 7(a)–(c)) multiply scattered signal in seeding-free regions is excluded from further processing using so-called not-a-number values (NaN, hatched area in schematic figure 7(a)). Pixels with NaN values are dummies which are not longer considered for any further mathematical operation in the processing. In the non-thresholded case (figure 7(d)) this signal is retained (light gray area) and mixed with particle information (dark gray area). This post-processing procedure is biasing temperatures additionally to the physical effect of mixing temperature information described in section 1. Within the exemplary interrogation area in the shear layer, the averaged temperature is $\overline{T} = 421$ K for the thresholded conventional (figure 7(a)) and $\overline{T} = 396$ K for the non-thresholded conventional (figure 7(d)). Here, the influence of multiple scattering appears to underestimate temperatures. However, this behavior is opposite in the jet core. Both the 2p- (figure 7(b)) and 1p-SLIPI (figure 7(c)) approach apparently overestimate jet temperature in the jet least of all (colored gray and white), indicating a higher accuracy than the conventional approach. The number of overestimated temperature samples increases for the conventional (figure 7(a)) and reaches its maximum for the non-thresholded conventional case (figure 7(d)). In the latter case, any multiple scattering and background signal in seeding-free areas is erroneously converted to strongly biased temperature. Accordingly, with a higher influence of multiple scattering the number of overestimated or underestimated temperatures rises in the presented cases. These findings are observed both

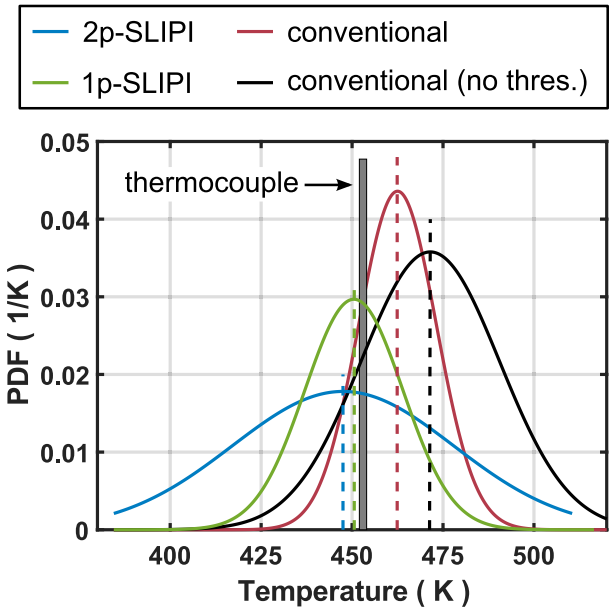

Figure 8. Probability density functions (PDF) for temperature information extracted from triangular regions in the jet core centers in figure 7. Experimental temperature distributions (not shown) are approximated by fitting a Gaussian distribution.

Table 1. Signal-to-noise ratio (SNR) values for different reconstruction approaches for both red and blue camera channel as well as jet and co-flow. Values given are peak values derived from the SNR distributions.

	Jet		Co-flow	
	Red	Blue	Red	Blue
2p-SLIPI	23	10	12	3.5
1p-SLIPI	24	16	10	4
Conv.	65	25	22	4
Conv. (no thres.)	47	18	3.5	1.5

globally (e.g. region ① in jet core) and for local flow structures (e.g. region ②). In accordance with section 5.1, local temperature gradients are well preserved applying the threshold algorithm.

To evaluate the different approaches in terms of temperature accuracy and precision, figure 8 shows probability density functions (PDF) that are extracted from a triangle area located in the jet core (triangle highlighted in figure 7(a)) where the temperature is homogeneous and unaffected by mixing (height of triangle $\approx 0.7 \cdot d_{\mathrm{jet}}$). To estimate accuracy, the difference between the jet core set-temperature of 453 K (measured by type K thermocouple) and the average temperature within the extracted triangle is used (peak of Gaussian-fitted distribution curve). The full width half maximum (FWHM) of the temperature distribution within the extracted triangle serves as a measure for precision. 1p- and 2p-SLIPI cases provide highest accuracies with systematic errors as low as 2 K and 4 K respectively. However, their precision of 35 K (1p) and 72 K (2p) is rather poor and suffers from minor SNR values, especially in the 2p-SLIPI approach. The conventional case features an intermediate accuracy with deviations of 14 K and a precision of 25 K. The non-thresholded conventional case possesses both a reduced accuracy (bias of 19 K) and precision (45 K). The signal unaffected by multiple scattering ($S_{\mathrm{un-scattered}}$) and multiply scattered intensity (S_{MS}) contribute to the total signal S. Consequently, the apparent SNR can be defined as

$$\mathrm{SNR} = \frac{S}{N} = \frac{S_{\mathrm{un-scattered}} + S_{\mathrm{MS}}}{N}. \qquad (3)$$

The noise N originating from the detection system, i.e. cameras, is considered for calculation here. It is not influenced by the image reconstruction. As both 1p- and 2p-SLIPI reduce multiple scattering, the signal S is reduced while $N = \mathrm{const.}$, resulting in lower apparent SNR values for these approaches. SNRs are further evaluated and results are summarized in table 1. For estimating noise, zone Ⓐ in figure 7(b) is utilized. The jet signal is extracted from the jet core (zone Ⓑ in figure 7(b)), while co-flow signal is taken from zone Ⓒ. Averaged values in the respective areas are used. As 2p-SLIPI is based on a subtractive reconstruction (section 2.2), it results in lowest overall signal intensities and therefore in lowest SNR values. For the 1p-SLIPI reconstruction only one sub-image is used, resulting in approximately half the overall available particle information for the image reconstruction compared to 2p-SLIPI. However, the 1p approach yields SNRs slightly better than those for 2p-SLIPI. The subtraction in 2p-SLIPI reconstruction balances the increased overall signal. In addition, using SLIPI, intensities are reduced by filtering lower frequency components, attributed to multiple scattering. SNRs in the conventional case are not affected by the SLIPI reconstruction procedure such that the SNRs are overall larger. However, for the non-thresholded conventional approach SNR values are weak in areas with sparse seeding. In the case considered here this is observed particularly in the co-flow region.

6. Summary and conclusion

In the present study structured laser illumination planar imaging (SLIPI) is combined with gas phase phosphor thermometry to derive quasi-instantaneous, two-dimensional temperature fields that are less biased by multiple scattering than conventional phosphor thermometry. 1p- and 2p-SLIPI are compared to the conventional approach and its advancement based on a gradient threshold removing areas without any seeding particles prior to further image processing. The main findings are summarized as follows:

(a) The non-thresholded conventional approach suffers from areas where no or varying amounts of seeding particles are present. This results in a low temperature sensitivity, a significant temperature bias (low accuracy) and low precision.
(b) Applying the gradient threshold algorithm removes areas containing any particles from post-processing. This reduces the impact of multiple scattering and improves accuracy, precision and temperature sensitivity. However, at high seeding densities the bias is not entirely avoided.
(c) 1p-SLIPI exhibits high accuracy at intermediate precision. Multiply scattered luminescence is not fully removed and, inherent to the 1p-SLIPI approach, spatial resolution is decreased. The experimental complexity is less than for 2p-SLIPI.
(d) 2p-SLIPI is recommended for high temperature sensitivity and accuracy, removing most reliably the impact of multiple scattering. As a significant shortcoming, 2p-SLIPI has lowest SNR accompanied by poor precision. To overcome this limitation, signal intensities particularly of the blue camera channel needs to be improved, for example by selecting different filter combinations. Another drawback of the 2p-SLIPI approach is its experimental complexity and costs. The optical alignment, however, can be greatly simplified using a calcite crystal approach [23].

In summary, SLIPI is a valuable approach significantly reducing multiple scattering in gas phase phosphor thermometry. SLIPI is mandatory for complex geometries with dense or spatial-temporally seeding fluctuations where the bias can not be easily corrected for by the calibration procedure. For sparse or constant seeding densities, specifically in canonical geometries, the influence of multiple scattering can be reduced by calibration using comparable seeding conditions as in the actual measurement and structured illumination may be not necessary.

Future studies using SLIPI-LIL for gas phase thermometry should focus on improving temperature precision and simplifying the experimental complexity. Also a further extension of SLIPI-LIL with a SLIPI-PIV approach, as shown in [30], appears very promising for simultaneous velocimetry.

Acknowledgments

The authors acknowledge generous funding by Deutsche Forschungsgemeinschaft (DFG) through Grants DR 374/16-1. Michael Stephan is financially supported by the Darmstadt Graduate School of Energy Science and Engineering (GSC 1070). Edouard Berrocal gratefully acknowledges the generous funding by the European Research Council (Agreement No 638546—ERC starting Grant 'Spray Imaging'). Andreas Dreizler is supported through the Wilhelm Leibniz program.

Appendix. Gradient threshold algorithm

The implementation of the gradient threshold algorithm is described in the following, according to the outlines in Stephan [34]. The particles are identified using approximations of the first and second order derivative of the image. The first derivative $\nabla\mathbf{f}$ of an image $f(x, y)$ is defined as

$$\nabla\mathbf{f} = \begin{pmatrix} G_x \\ G_y \end{pmatrix} = \begin{bmatrix} \frac{\partial f}{\partial x} \\ \frac{\partial f}{\partial y} \end{bmatrix}, \tag{A.1}$$

where G_x and G_y are the gradient components and the vector $\nabla\mathbf{f}$ points into the direction of maximal local intensity change in f. Especially, for purposes of image processing and edge detection, the magnitude ∇f_{Mag} is important:

$$\nabla f_{\text{Mag}} = \text{mag}(\nabla\mathbf{f}) = \sqrt{G_x^2 + G_y^2}. \tag{A.2}$$

For numerical implementation, the two dimensional domain shown in figure A1 is used. The gradients are approximated based on a procedure of Prewitt and Sobel, outlined in Gonzalez and Woods [33]:

$$G_x = (z_7 + 2z_8 + z_9) - (z_1 + 2z_2 + z_3) \tag{A.3}$$

and

$$G_y = (z_3 + 2z_6 + z_9) - (z_1 + 2z_4 + z_7). \tag{A.4}$$

These equations base on a 3×3 pixel environment centered at z_5 (see figure A1). Accordingly, the magnitude of the gradient ∇f_{Mag} is numerically approximated by

$$\nabla f_{\text{Mag}} \approx |G_x| + |G_y|. \tag{A.5}$$

For particle identification, the approximated magnitudes of the gradient are thresholded with $\nabla f_{\text{Mag}} > T_1$ with $T_1 = \overline{\nabla f_{\text{Mag}}}$. The operation $\overline{X}$ stands for spatial averaging of the whole image domain X. In doing so, particle centers are originally excluded, as the gradient is decreasing below T_1 when approaching individual particle centers. This is compensated by application of an additional mask, in turn, including centers. If $\nabla f_{\text{Mag}}(z_i) > T_1$ for more than four values $z_i \in \{z_1, ..., z_4, z_6, ..., z_9\}$ in the 3×3 pixel environment (figure A1), the corresponding center z_5 is considered, i.e. included in the mask, despite the gradient's magnitude of z_5 is too low ($\nabla f_{\text{Mag}}(z_5) < T_1$). In addition to the magnitude of gradients, information of the second order derivative is required to determine if the detected extrema are maximum or minimum. For this purpose, the Laplacian of $f(x, y)$

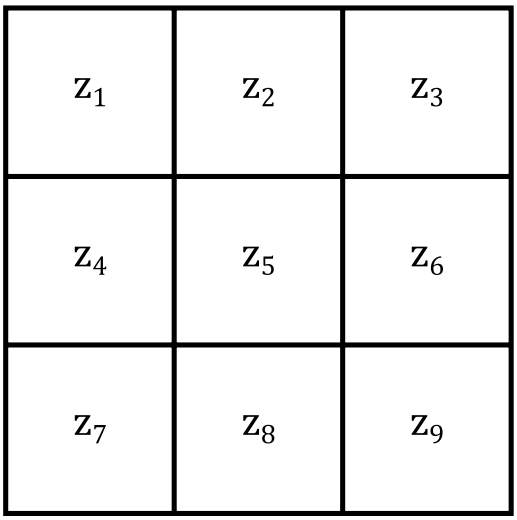

Figure A1. 3×3 pixel environment with center z_5.

$$\Delta f = \nabla^2 f = \frac{\partial^2 f}{\partial x^2} + \frac{\partial^2 f}{\partial y^2} \tag{A.6}$$

is used, and approximated numerically by:

$$\nabla^2 f = 8z_5 - (z_1 + z_2 + z_3 + z_4 + z_6 + z_7 + z_8 + z_9). \tag{A.7}$$

Again, a threshold $T_2 = \overline{\Delta f}$ is applied for identification. Consequently, regions with $\Delta f > T_2$ are considered to belong to particles. The sole utilization of second order derivative information is not recommended, as it is very sensitive to high noise levels [33]. For more detailed information it is referred to Gonzalez and Woods [33] as well as Stephan [34].

ORCID iDs

Florian Zentgraf https://orcid.org/0000-0003-1845-0184

References

[1] Kucsko G, Maurer P C, Yao N Y, Kubo M, Noh H J, Lo P K, Park H and Lukin M D 2013 Nanometre-scale thermometry in a living cell *Nature* **500** 54–8

[2] Qiao J, Mu X and Qi L 2016 Construction of fluorescent polymeric nano-thermometers for intracellular temperature imaging: a review *Biosens. Bioelectron.* **85** 403–13

[3] Allison S W, Baker E S, Lynch K J and Sabri F 2017 *In vivo* x-ray excited optical luminescence from phosphor-doped aerogel and sylgard 184 composites *Radiat. Phys. Chem.* **135** 88–93

[4] Roy S, Gord J R and Patnaik A K 2010 Recent advances in coherent anti-stokes raman scattering spectroscopy: fundamental developments and applications in reacting flows *Prog. Energy Combust. Sci.* **36** 280–306

[5] Miles R B, Lempert W R and Forkey J N 2001 Laser rayleigh scattering *Meas. Sci. Technol.* **12** R33

[6] Liu X, Jeffries J B, Hanson R K, Hinckley K M and Woodmansee M A 2006 Development of a tunable diode laser sensor for measurements of gas turbine exhaust temperature *Appl. Phys.* B **82** 469–78

[7] Schulz C and Sick V 2005 Tracer-LIF diagnostics: quantitative measurement of fuel concentration, temperature and fuel/air ratio in practical combustion systems *Prog. Energy Combust. Sci.* **31** 75–121

[8] Aldén M, Omrane A, Richter M and Särner G 2011 Thermographic phosphors for thermometry: a survey of combustion applications *Prog. Energy Combust. Sci.* **37** 422–61

[9] Brübach J, Pflitsch C, Dreizler A and Atakan B 2013 On surface temperature measurements with thermographic phosphors: a review *Prog. Energy Combust. Sci.* **39** 37–60

[10] Abram C, Fond B and Beyrau F 2018 Temperature measurement techniques for gas and liquid flows using thermographic phosphor tracer particles *Prog. Energy Combust. Sci.* **64** 93–156

[11] Fond B, Abram C, Heyes A L, Kempf A M and Beyrau F 2012 Simultaneous temperature, mixture fraction and velocity imaging in turbulent flows using thermographic phosphor tracer particles *Opt. Express* **20** 22118–33

[12] Lee H, Böhm B, Sadiki A and Dreizler A 2016 Turbulent heat flux measurement in a non-reacting round jet, using BAM:Eu^{2+} phosphor thermography and particle image velocimetry *Appl. Phys.* B **122** 209

[13] Stephan M, Lee H, Albert B, Dreizler A and Böhm B 2016 Simultaneous planar gas-phase temperature and velocity measurements within a film cooling configuration using thermographic phosphors *18th Int. Symp. on the Application of Laser and Imaging Techniques to Fluid Mechanics (Lisbon, Portugal)*

[14] Schreivogel P, Abram C, Fond B, Straußwald M, Beyrau F and Pfitzner M 2016 Simultaneous kHz-rate temperature and velocity field measurements in the flow emanating from angled and trenched film cooling holes *Int. J. Heat Mass Transfer* **103** 390–400

[15] Särner G, Richter M and Aldén M 2008 Investigations of blue emitting phosphors for thermometry *Meas. Sci. Technol.* **19** 125304

[16] Lindén J, Takada N, Johansson B, Richter M and Aldén M 2009 Investigation of potential laser-induced heating effects when using thermographic phosphors for gas-phase thermometry *Appl. Phys.* B **96** 237–40

[17] van Lipzig J P J, Yu M, Dam N J, Luijten C C M and de Goey L P H 2013 Gas-phase thermometry in a high-pressure cell using $BaMgAl_{10}O_{17}$:Eu as a thermographic phosphor *Appl. Phys.* B **111** 469–81

[18] Zentgraf F, Stephan M, Berrocal E, Albert B, Böhm B and Dreizler A 2017 Application of structured illumination to gas phase thermometry using thermographic phosphor particles: a study for averaged imaging *Exp. Fluids* **58** 82

[19] Berrocal E, Kristensson E, Richter M, Linne M and Aldén M 2008 Application of structured illumination for multiple scattering suppression in planar laser imaging of dense sprays *Opt. Express* **16** 17870

[20] Kristensson E, Berrocal E, Richter M, Pettersson S-G and Aldén M 2008 High-speed structured planar laser illumination for contrast improvement of two-phase flow images *Opt. Lett.* **33** 2752

[21] Kristensson E, Berrocal E, Richter M and Aldén M 2010 Nanosecond structured laser illumination planar imaging for single-shot imaging of dense sprays *Atomization Sprays* **20** 337–43

[22] Kristensson E, Berrocal E and Aldén M 2014 Two-pulse structured illumination imaging *Opt. Lett.* **39** 2584–7

[23] Storch M, Mishra Y N, Koegl M, Kristensson E, Will S, Zigan L and Berrocal E 2016 Two-phase SLIPI for instantaneous LIF and Mie imaging of transient fuel sprays *Opt. Lett.* **41** 5422–5

[24] Mishra Y N, Kristensson E, Koegl M, Jönsson J, Zigan L and Berrocal E 2017 Comparison between two-phase and one-phase SLIPI for instantaneous imaging of transient sprays *Exp. Fluids* **58** 110

[25] Berrocal E, Johnsson J, Kristensson E and Aldén M 2012 Single scattering detection in turbid media using single-phase structured illumination filtering *J. Eur. Opt. Soc.: Rapid Publ.* **7** 12015

[26] Mishra Y N, Kristensson E and Berrocal E 2014 Reliable LIF/Mie droplet sizing in sprays using structured laser illumination planar imaging *Opt. Express* **22** 4480–92

[27] Mishra Y N, Abou Nada F, Polster S, Kristensson E and Berrocal E 2016 Thermometry in aqueous solutions and sprays using two-color LIF and structured illumination *Opt. Express* **24** 4949–63

[28] Kempema N J and Long M B 2014 Quantitative rayleigh thermometry for high background scattering applications with structured laser illumination planar imaging *Appl. Opt.* **53** 6688–97

[29] Kristensson E, Ehn A, Bood J and Aldén M 2015 Advancements in rayleigh scattering thermometry by means of structured illumination *Proc. Combust. Inst.* **35** 3689–96

[30] Kristensson E and Berrocal E 2018 Crossed patterned structured illumination for the analysis and velocimetry of transient turbid media *Sci. Rep.* **8** 11751

[31] Gustafsson M G L 2005 Nonlinear structured-illumination microscopy: wide-field fluorescence imaging with theoretically unlimited resolution *Proc. Natl Acad. Sci. USA* **102** 13081–6

[32] Kristensson E 2012 Structured laser illumination planar imaging—SLIPI: applications for spray diagnostics *PhD Thesis* Lund University, Lund

[33] Gonzalez R C and Woods R E 2002 *Digital Image Processing* 2nd edn (Upper Saddle River, NJ: Prentice-Hall)

[34] Stephan M 2018 Anwendung und entwicklung von laserinduzierter phosphorthermometrie zur bestimmung von fluidtemperaturen *PhD Thesis* Technische Universität Darmstadt, Darmstadt